Materials Today Quantum 6 (2025) 100043

Contents lists available at ScienceDirect

Materials Today Quantum

journal homepage: www.sciencedirect.com/journal/materials-today-quantum

Innovative direct manufacturing of tungsten carbide superconducting nanowires for photon detection applications via pulsed focused ion beam induced deposition

Cristina García-Pérez [a], Fernando J. Urbanos [a], Gabriel Caballero [a], Manuel R. Osorio [a], Alicia Gómez [b], Ramón Bernardo-Gavito [a], Daniel Granados [a,c,*]

[a] IMDEA Nanociencia, Faraday, 9, Madrid 28049, Spain
[b] Centro de Astrobiología (CAB) CSIC-INTA, Ctra. Torrejón-Ajalvir km.4, Madrid 28850, Spain
[c] Unidad de Nanomateriales Avanzados, IMDEA-Nanociencia, Unidad Asociada al CSIC por el ICMMC/ Faraday 9, 28049 Madrid, Spain

ARTICLE INFO

Keywords:
Tungsten carbide
Superconducting nanowires
FIBID
Photon detection
SNSPD
Quantum sensing

ABSTRACT

We present the development and optical characterization of tungsten carbide superconducting nanowire devices for photon detection. They are nanofabricated by direct deposition via pulsed focused ion beam induced deposition (PFIBID) using Tungsten Hexacarbonyl ($W(CO)_6$) as precursor. The nanowires exhibit a critical temperature of 4.71 K and demonstrate a notable response to low-intensity CW or pulsed laser illumination. For the first time, in-operando photoresponse low-temperature maps reveal hotspot distributions under low power illumination and localized superconductivity suppression upon high fluence photon absorption at higher powers. Dynamic response measurements under 1 MHz repetition rate, 640 nm pulsed laser excitation highlight the fast temporal response of the detectors and high operation stability near saturation. While currently operating in the multi-photon regime (9 photons/output-pulse), the findings emphasize their potential for single-photon detection with further optimization of material thickness (target <25 nm) and excitation schemes. This work demonstrates the significant promise to direct nanofabricate superconducting devices based on WC for advanced quantum applications.

1. Introduction

Superconductivity is a unique electronic state of matter attained under specific conditions of temperature, magnetic field, and applied current, where the material exhibits zero electrical resistance [1]. The non-dissipative regime is an appealing framework for the design of advanced quantum technology devices such as nano-resonators [2], superconducting quantum interference devices (SQUIDs) [3], quantum switches [4], logic gates [5], quantum bits based on phase slip centers [6] and superconducting single-photon detectors [3,7,8]. When the dimensions of a device are reduced to the scale or below of the superconducting characteristic lengths of the material novel physical phenomena emerge, absent in macroscopic systems [9].

One glaring example is the development of Superconducting Nanowire Single-Photon Detectors (SNSPDs). In these devices, a superconductor is nanopatterned to achieve confinement below its critical length scale in at least one dimension, enabling the emergence of unique physical phenomena. They operate by applying a bias current (I_b) slightly below the critical current (*typically around* $0.9I_c$). Under illumination with an energy above the superconducting gap, a photon can be absorbed, creating a localized resistive hotspot that forces the current to exceed I_c in the surroundings of the hot-spot, which then grows due to negative electrothermal feedback. This forces I_b to momentarily divert through the external shunt circuit, generating a measurable voltage pulse [3] (Fig. 1). The production of SNSPDs has traditionally relied on well-established nanofabrication techniques such as electron beam lithography (EBL), optical lithography, lift-off, and reactive ion etching. While these methods offer compatibility with very large-scale integration, they are costly and prone to errors and defects, limiting their practicality in research and development applications. However, the onset of focused ion beam induced deposition (FIBID) offers a promising alternative, avoiding the need for resists and solvents [1,5,10] (hence avoiding contamination and damage) while maintaining flexible patterning with high precision [1,5,10] and lateral resolution compared

* Corresponding author at: IMDEA Nanociencia, Faraday, 9, Madrid 28049, Spain.
E-mail address: daniel.granados@imdea.org (D. Granados).

https://doi.org/10.1016/j.mtquan.2025.100043
Received 16 January 2025; Received in revised form 21 March 2025; Accepted 22 April 2025
Available online 26 April 2025

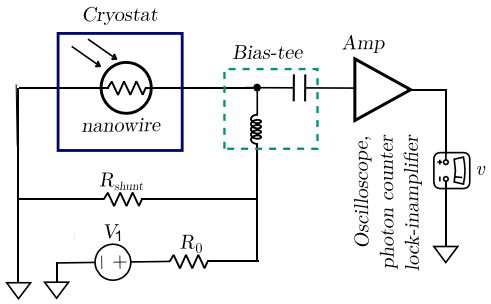

Fig. 1. Diagram of the electronic set-up for low-temperature measurements. The set-up includes a bias circuit and a readout circuit.

to structures defined by EBL [11]. Unlike multi-step lithography, FIBID enables single step [12] in situ patterning without masks [13]. Moreover, together with the clean growth [5], the combination of imaging during the fabrication process [14,15] and the possibility of modifying parts of the design simultaneously to the growth [10] has led to the wide use of this technique in the semiconductor industry [14,16–18], and have recently drawn significant interest for producing superconducting components [19,20] in advanced nanodevices [5].

The FIBID process (Fig. 2) can be considered as a chemical vapor deposition process assisted by an ion beam [14]. A focused ion beam, typically Ga+ , induces the dissociation of gas-phase precursor molecules absorbed on the substrate surface [1,7,11], producing both volatile and non-volatile constituents [1]. The volatile products are removed via the instrument's vacuum system [20], while the non-volatile by-products form a nano-deposit along the path of the ion beam [5] which is scanned with a pattern generator in the desired shape [1]. The number of loops and dwell time allow to control the thickness and width of the final deposit. In this research we use pulsed-FIBID instead of FIBID. PFIBID uses a pulsed beam instead of a continuous beam, allowing time for the precursor gas to replenish and for the byproducts to be removed between pulses. This results in higher purity deposits, reduced sample damage, and better structural control[1].

The FIBID deposition technique has been employed to deposit a variety of metallic and insulating materials [10,14,21] and in the last few decades it has been successfully used to fabricate low dimensional superconducting materials including tungsten [20]. Tungsten-based materials, particularly those deposited using the tungsten hexacarbonyl ($W(CO)_6$) precursor, exhibit superconducting properties and are stable and resistant to aging under ambient conditions [14]. These deposits present figures of merit comparable to other superconducting materials and to W-based deposits produced with other physical vapor deposition methods [1,7]. In the literature, WC deposits fabricated via FIBID exhibit critical temperatures (T_c) ranging from 4 to 5 K [1,22], which is up to two orders of magnitude higher than that of crystalline tungsten [1,11,21,22]. While the exact superconducting mechanism of WC deposited by FIBID remains unclear, it is hypothesized to arise from its amorphous, disordered structure, stabilized by carbon content and Ga implantation, with the high density of defects playing a critical role [10, 23].

Since FIBID WC deposits exhibit a higher T_c than many other metallic superconductors [5], they are strong candidates for the fabrication of superconducting nanodevices [5]. It has been suggested that WC-FIBID deposits could potentially be used as SNSPDs [24]. However, to our knowledge, their response to light at low temperatures of tungsten carbide has not been experimentally characterized until now. In this research, we fabricated tungsten carbide nanowires using Pulsed-FIBID and, for the first time, studied their response to pulsed illumination at low-intensity laser power. Among their superconducting and detection properties, we present the first in-operando photoresponse low-temperature maps, with nanometer-scale lateral resolution, enabling the visualization of hotspot distributions. While the single-photon detection regime has not yet been experimentally achieved, our work successfully demonstrates the potential of WC deposited in this approach for the development of SNSPDs, as well as other superconducting devices with potential applications for quantum technologies.

2. Experimental

All samples were fabricated on N^{++} doped Silicon (001) substrates with a 290 nm-thick thermal SiO_2 layer on the surface. Prior to WC deposition onto the SiO_2 layer and following procedures similar to those used by other research groups [20], Ti/Au contacts (100-nm thick Au/Ti bilayer) were patterned using optical maskless laser UV lithography, e-beam evaporation for the metallic bilayer, and a lift-off process and acetone, IPA and DI-water. The Ti/Au pads were arranged in a four-probe configuration for transport measurements.

WC nanowires were fabricated at room temperature using a dual-beam SEM/FIB system (Carl Zeiss Auriga) equipped with a Ga+ ion source [23] and a Gas Injection System (GIS) with a tungsten hexacarbonyl ($W(CO)_6$) precursor reservoir. The precursor was injected via a gas nozzle to create a localized high-pressure region for site-specific tungsten deposition. The ion beam was rastered over the substrate using a 14-bit per axis, 400 MHz-DSP pattern generator (Raith Multibeam), ensuring precise nanostructure definition. The resulting non-volatile deposits, composed of W, C, and small amounts of Ga and O

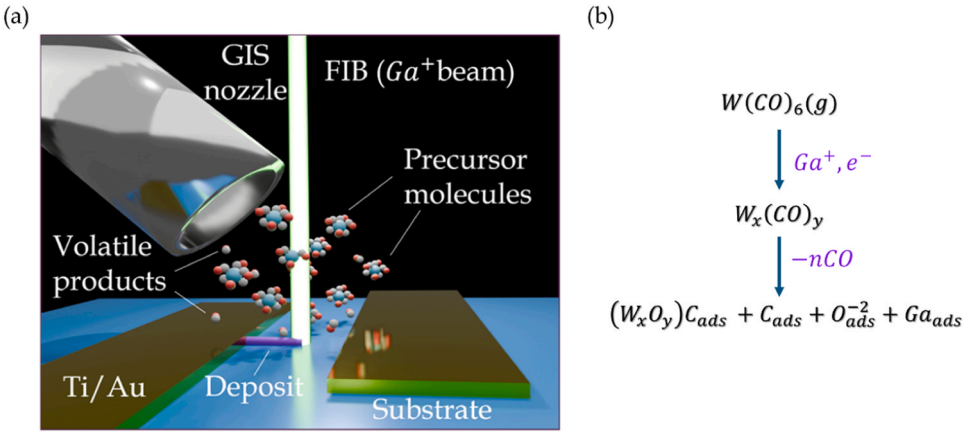

Fig. 2. (a) Illustration of the nanowire fabrication by Pulsed-FIBID using Ga^+ ions. The beam of Ga^+ ions is focused on an insulating substrate (SiO_2/Si) while a W $(CO)_6$ gas flow is injected in the vicinity of the beam from gas injection nozzle. (b) Representation of the reaction, products, and by-products generated during the interaction between the tungsten hexacarbonyl precursor ($W(CO)_6$) and the Ga^+ focused ion beam (FIB) for the deposition of the WC nanowires.

impurities, formed the nanowires in between the Ti/Au pads (see Fig. 6).

The FIB energy used is 30 keV, with a Ga^+ beam current of 50 pA. During the deposition, the system beam equivalent pressure (BEP) is kept at 2.10^{-5} mbar while the injection precursor gas is flowing in the vicinity of the TiAu pads. The distance between the nozzle and the surface is circa 200 μm and the nozzle is center in between the contacts gap. Magnification of both SEM and FIB guns is set at 500x, allowing the patterning of structures within a 100×100 μm^2 write field window. Deposition conditions are summarized in Table 1. Thereafter, samples are inspected via Atomic Force Microscopy, Field Emission Scanning Electron Microscopy (FE-SEM), Optical Microscopy, Energy Dispersive Spectroscopy and electrically characterized in a probe station. Some of the chips with the devices are electrically contacted in a chip carrier holder using ultrasonic Au-wire wedge bonding for optical and low temperature characterization.

The nanomanufactured nanowires are 20 μm long, 150 ± 40 nm wide (determined by FE-SEM in-situ immediately after deposition), and with a thickness of 50 ± 10 nm, as revealed by AFM measurements performed in contact mode using a Park XE7 AFM-MFM system (See Fig. 3b). FE-SEM images and AFM profiles, presented in Fig. 3, illustrate the dimensions and surface morphology of the WC nanowires.

The chemical composition analysis was conducted using energy-dispersive X-ray spectroscopy (EDS XL-30 Flash-Bruker) integrated into an Ultra High-Resolution FE-SEM (Carl Zeiss SIGMA with a Gemini column). Measurements were performed with an accelerating voltage of 15 kV and an EDS detector operating at −20 °C. The analysis revealed that the deposits consist of approximately 26 at% C, 18.7 at% W, 10.4 at % Ga, and 44.5 at% O. The oxygen content is most likely attributed to oxidation occurring after the nanowires were exposed to air upon removal from the FIB/SEM/GIS vacuum chamber.

The low-temperature electrical characterization was performed in a closed-cycle helium cryostat (attoDry 800 from AttoCube GmbH) with a base temperature of 3.8 K (± 10 mK), equipped with optical, DC, and RF ports. The cryostat features XYZ positioners and XYZ scanners, enabling the acquisition of low-temperature optical maps while applying or measuring DC or RF signals. Measurements from 300 K to 3.8 K were carried out using a Keithley 2450 Source-meter in a two-point probe configuration. For Resistance vs Temperature (R vs T) measurements, a fixed bias current of 1 μA was applied, and the bias voltage was recorded during cooling or heating ramps. Data acquisition was fully automated via Python scripts. The dynamic response to light was analyzed using a 640 nm (± 10 nm) pulsed laser at a 1 MHz repetition rate, attenuated to ~600 pW optical power (measured at the cryostat entrance). The light was delivered through a single-mode fiber and then propagated in free space to the cryostat's optical window. A gaussian beam profile was focused onto the device surface using an x80

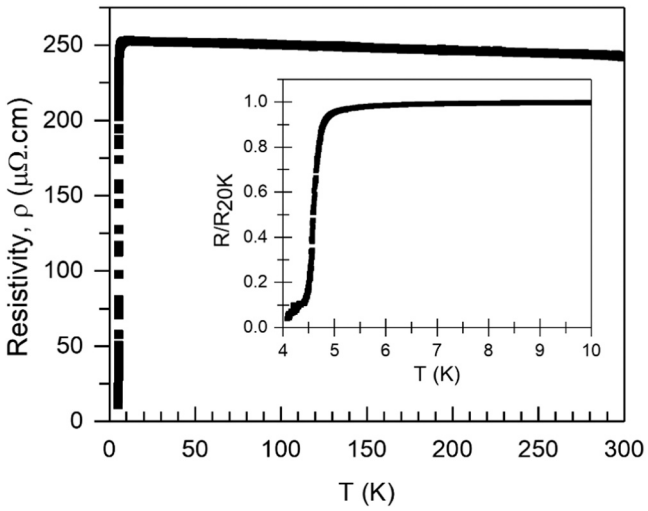

Fig. 4. Temperature dependence of the resistivity $\rho(T)$ of a WC-based nanowire at zero magnetic field. The normalized resistance is shown at the inset, where the resistivity at 20 K has been used for the normalization of the curve. The driving current is set to 1 μA during the temperature ramp. The inset shows a magnified view of the superconducting transition in the low-temperature region (4–10 K).

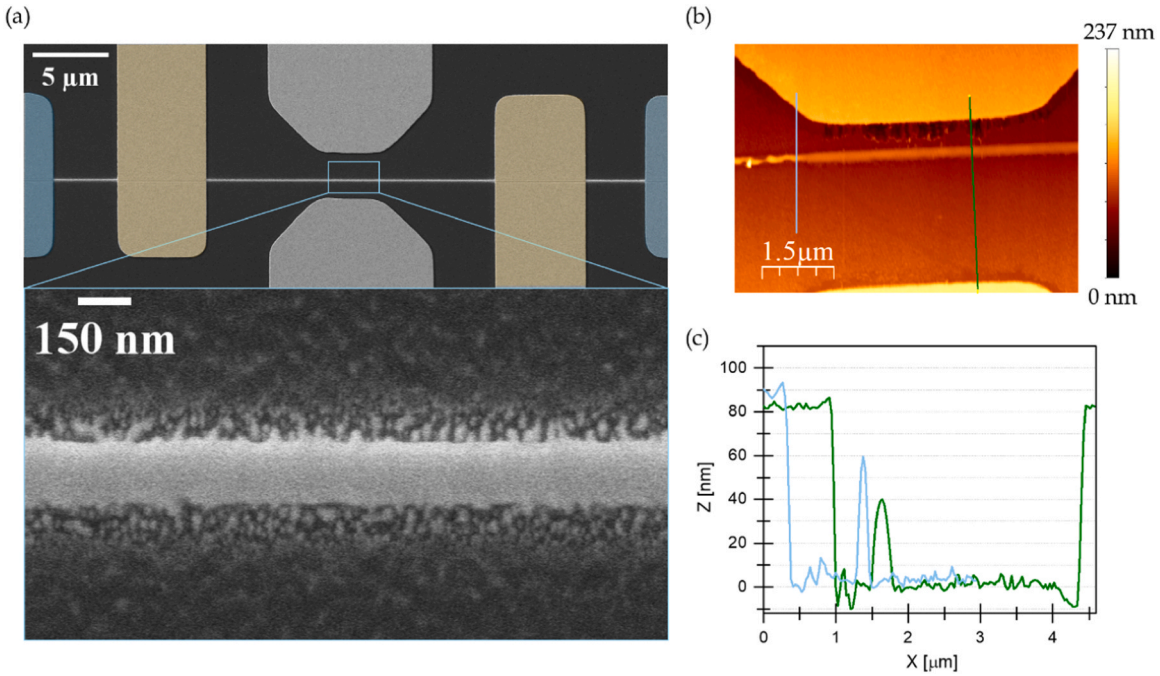

Fig. 3. (a) Top view is false colored Field Emission SEM image of a Ga^+ FIBID-deposited tungsten carbide nanowire connected to the Au/Ti pads on a SiO_2/Si substrate. Blue contacts are for current injection and gold ones for voltage measurement, following a four-point contact configuration. The bottom shows a zoom-in section of the nanowire (b) AFM image of the nanowire. The thickness is shown in the height profile (c). The nanowire dimensions are 20 μm long, 150 nm wide, and 50 nm thick.

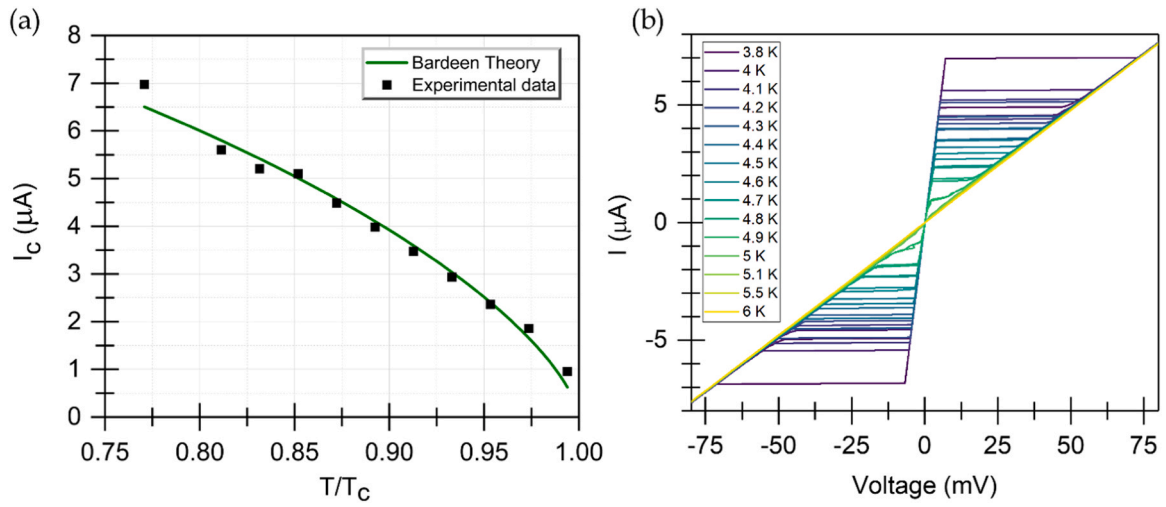

Fig. 5. (a) Critical current values (I_c) plotted as a function of temperature extracted from a set of current-voltage characteristics for the 50-nm-thick nanowire. The data follows the phenomenological prediction by Bardeen $I_c = \frac{1}{2\sqrt{2}} I_{c0} \left(1 - \left(\frac{T}{T_c}\right)^2\right)^{2/3}$ (green curve). (b) Hysteretic current-voltage characteristics of the nanowire at several temperatures ranging from 3.8 K to 6 K employed for the generation of the data shown in (a).

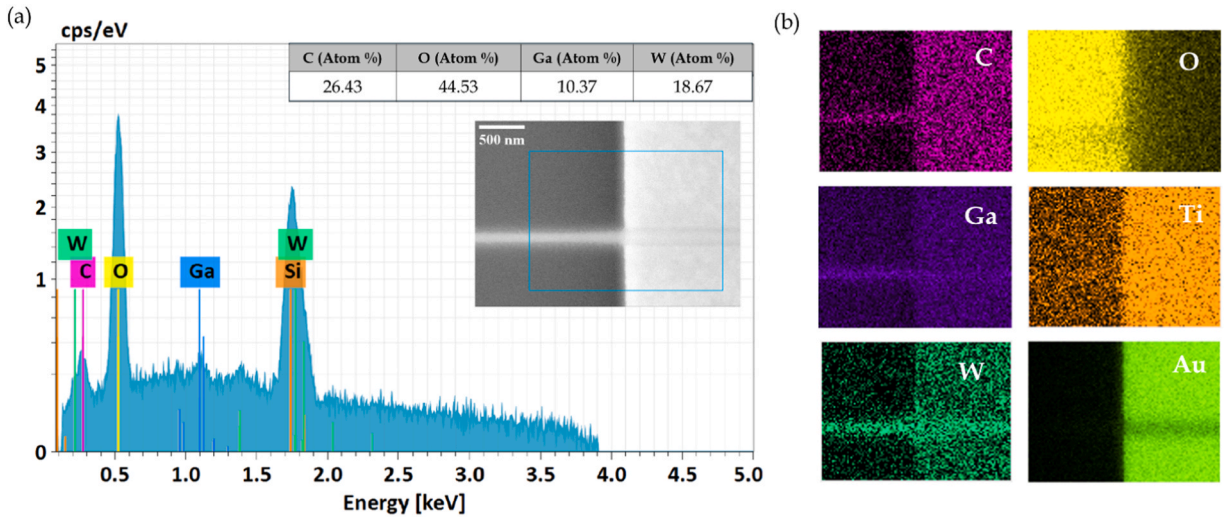

Fig. 6. (a) A typical EDX spectrum of a WC-FIBID nanowire on SiO_2/Si substrate. The inset of the spectrum shows the elemental ratio of the FIB deposited nanowire in atomic percentage and a FE-SEM image of the nanowire on top of the SiO_2/Si substrate and the Ti/Au contact. (b) EDX maps of each element. The results are the average obtained from the scanned area shown in blue in the SEM inset of (a).

Table 1
Deposition parameters of the samples.

Deposition conditions Ga^+ FIBID	
Precursor	$W(CO)_6$
Ion source	Ga^+
Acceleration voltage (kV)	30
Beam current (pA)	50
System pressure (mbar)	2.10^{-5}
Gun vacuum (mbar)	1.10^{-10}
Number of loops	50000
Dose per loop	5 $\mu C/cm^2$
Dwell time (μs)	92

apochromatic LT objective, obtaining a diffraction-limited spot of approximately one micron diameter. Reflectivity maps, micro-Raman, or micro-PL signals could be acquired simultaneously in a through-the-lens configuration using dichroic mirrors, beam splitters, and a CCD camera. Additional losses are expected through windows and the objective until they reach the sample. The calculations for photon losses through the cryostat system were performed to determine the number of photons ultimately absorbed by a nanowire detector, starting from the initial measured laser power. Key loss mechanisms were considered at each stage of the optical path. First, the laser beam, with a Gaussian profile, passes through two quartz windows on the cryostat. Each window introduces a reflectivity loss, calculated based on the refractive index of quartz at 640 nm, resulting in a total transmittance of 86.92 % through both windows. Next, the beam encounters the microscope objective, where only the central portion of the Gaussian beam (60.37 %) enters the objective due to the pupil limitation (3.4 mm diameter versus the incoming 5 mm beam). The objective itself has a transmission efficiency of 85 %. After passing through the objective, the focused Gaussian spot is projected onto the nanowire detector, which has a width of 100 nm. Considering the Gaussian intensity distribution of the spot (approximately 571.8 nm radius), only 1.52 % of the photons are geometrically aligned to interact with the nanowire. Further, the

nanowire's material, tungsten carbide (WC), has a reflectivity of 50 %, and the remaining photons experience internal absorption following Beer-Lambert's law, resulting in a 25.92 % absorption efficiency. Overall, the cumulative efficiency from initial laser power to photons absorbed by the nanowire is calculated by combining these sequential losses, allowing estimation of the effective photon count that can trigger detection events, given a quantum efficiency of 10 % for generating detectable responses in the nanowire.

The electronic setup, commonly used in SNSPD measurements, is illustrated in Fig. 1. The bias current is applied through the DC port of the bias-tee (Mini-Circuits ZFBT-4RGW 0.1–4200 MHz), while voltage pulses are read out via the AC port, amplified with a room-temperature 40-dB low-noise amplifier (Femto, DUPVA-1–70), and then routed to an oscilloscope (R&S MXO4 - 500 MHz) or a multipurpose FPGA-based Moku instrument (MokuLab). The MokuLab can operate as a lock-in amplifier or as a time-correlated single-photon counter. To prevent detector latching, a shunt resistor (R_{shunt}) of 50–100 Ω is connected in parallel with the nanowire. The AC lock-in amplifier module of the Moku instrument, combined with the nano-positioners and scanner, enables the acquisition of photoresponse maps with spatial resolution down to tens of nanometers, as well as diffraction-limited reflectivity maps with sub-micron resolution.

3. Discussion

The electrical transport properties of WC-FIBID nanowires fabricated by Ga^+ Pulsed-FIBID were analyzed through temperature-dependent electrical measurements. For critical temperature (T_c) determination, a constant current of 1 μA was applied and voltage was measured between the two inner terminals. For clarity, the resistance has been normalized to the nanowire resistance at 20 K. The T_c determination was based considering the temperature at which the resistance drops to 50 % of the resistance value at 20 K, and the transition width (ΔT_c) was defined similarly, as the temperature range where the resistance decreases from 90 % to 10 % of its value at 20 K, following a standard criterion for superconductor characterization. Fig. 4 illustrates a typical example of the superconducting transition observed in one of the nanowires. Below T_c, a sharp drop in resistance is observed, indicating a clear superconducting phase. The WC manufactured nanowires exhibit a superconducting transition at an average T_c of 4.71 ± 0.15 K and a width transition of 0.82 ± 0.28 K.

Considering the device dimensions obtained by SEM and AFM, the nanowires exhibit a room-temperature resistivity of 243 ± 44 μΩ·cm. This value is higher than the 5 μΩ·cm resistivity of bulk tungsten and consistent with the reported values for FIBID nanowires from the same precursor [10,19,20,23,25,26]. This increased resistivity is attributed to the presence of impurities inherent to the FIBID process, including carbon and oxygen introduced from the precursor gas and subsequent atmospheric oxidation [20]. The presence of impurities is also corroborated by the non-metallic behavior in the normal state as the temperature coefficient of resistivity $d\rho/dT$ is negative during the cool down, and even increasing its amplitude just before the superconducting transition, demonstrating impurity-dominated transport [21]. This deviation from metallicity, with a residual-resistivity ratio at 10 K ($\rho_{300K}/\rho_{10K} = 0.96$) is in line with other research [5] and consistent with scattering from C, Ga, O, and a high density of defects introduced during the FIBID process [5,22,27–32].

Moreover, as T_c is in the vicinity of 4.5 K and ΔT_c are comparable to similar studies [7,10,22,33], according to the BCS theory, the superconductivity bandgap would be $2\Delta_0 = 3.52 k_B T_c = 1.43\ meV$. However, this must be checked by measuring the tunneling conductance as the prefactor of 3.52 can be smaller because of the weak coupling [1,14]. In any case, this value corresponds to the microwave range of the electromagnetic spectrum, close to the far-infrared region. Therefore, the detection efficiency (DE) is expected to be maximum at this wavelength because of the photon energy matching to the superconducting bandgap.

On the other hand, the coherence length of a Cooper pair ξ_{GL}, allows a rough estimation of the length scale on which superconductivity takes place in WC nanowires [13], being the most common value reported $\xi_{GL} \sim 6.25$ nm. Comparing this value to the Pippard's coherence length $\varepsilon_0 = \frac{\hbar v_F}{\pi \Delta}$, with a Fermi velocity $v_F \sim 5.10^5 m/s$, it can be concluded that the nanowire is in the dirty limit with $\xi = (l\varepsilon_0)^{1/2} < \varepsilon_0$ [21].

The samples show superconducting behavior, albeit with some residual resistance [23]. A significant residual resistance, amounting to 7.4 % of the normal state value at 3.8 K, was observed. The resistive tail below below T_c can be attributed to several factors. Firstly, since the T_c is close to the base temperature of the cryostat, part of this residual resistance at low temperatures indicates that the superconducting transition is not fully complete, meaning the superconductivity path is not entirely percolating [23]. Additionally, it may arise from various dissipation mechanisms in the superconductor, such as phase-slip-driven processes, vortex-antivortex proliferation, and the presence of microstructural defects or disorders [21,24,34,35].

It is worth noting that, although W is a type I superconductor, WC fabricated by FIBID behaves as a type II conventional superconductor due to its finite thickness, amorphous structure, and high density of defects. This allows for the formation of hexagonally distributed Abrikosov vortices. Structural disorder, multi-grain domains, and scattering defects act as pinning centers for these vortices [1,14,36]. Additionally, even in the quasi-2D limit, a competition between phase-slip mechanisms and flux proliferation has been reported, governed by vortex dynamics [24]. These effects become more pronounced in 1D-like systems where the width is comparable to the coherence length ($\xi \sim w$). However, it has been verified that even for $w/\xi \sim 100$, the formation of phase slip strips (PSSs) and the LAMH theory are still applicable [24,37,38]. In our case, both the thickness ($t/\xi \sim 8$) and the width ($w/\xi \sim 24$) are substantially higher than ξ, placing our nanowires in the quasi 2D limit, with $w/\xi \sim 24$.

The resistance below T_c has several components: $R = R_c + \left\{ R_N^{-1} + (R_{TAPS} + R_{QPS})^{-1} \right\}^{-1}$. Where R_c is the resistance contribution coming from the Au/Ti contact pads, which come in series with the nanowire. R_N is the normal state resistance arising out of the quasiparticle's contributions (uncomplete transition), R_{TAPS} is the resistance associated to thermally activated phase slips (dominant near T_c) and R_{QPS} is the quantum phase slips resistance (present throughout the temperature range). Nevertheless, inhomogeneities, disorder, metallic grains behaving as Josephson junctions, can also contribute to the residual resistance [24]. The broadening of the superconducting transition can also be accounted for by the occurrence or phase slips, and by the presence of local constrictions, either on the long axis of the nanowire or on the crossing points with transversal leads [7].

The presence of phase slips was further corroborated by the hysteretic IV characteristics and the stochastic distribution of the critical currents [21,39–43]. The nanowire remains superconducting up to a critical de-pairing current I_c and shows hysteretic behavior. Heating effects are crucial in defining the hysteretic behavior [21]. The effects of thermal hysteresis and the subsequent latching can be mitigated or even totally suppressed using a shunt resistor (S1). The critical current density at 3.8 K was estimated from the I-V curve and the geometric parameters yielding $J_c \sim (0.93 \pm 0.36).10^5 A/cm^2$, comparable to other WC-FIBID nanowires [5].

An ensemble of current-voltage characteristic as a function of temperature is shown at Fig. 5. The experimental results show a very good fit to the phenomenological prediction by Bardeen [44]. This fit suggests a I_{c0} close to 33 μA, in good agreement with other groups [5].

$$I_c = \frac{1}{2\sqrt{2}} I_{c0} \left(1 - \left(\frac{T}{T_c} \right)^2 \right)^{2/3} \quad (1)$$

Fig. 6 shows the EDX analysis, which confirms the presence of W, C, O and Ga. This is congruent to the decomposition of the organometallic

compound precursor [7,21], with atomic concentrations of about 18.7 %, 26.4 %, 44.5 %, and 10.37 %, for W, C, O and Ga, respectively. W exhibits characteristic lines in the M series, including W-Mα (1.775 keV), W-Mβ (1.945 keV), and W-Mγ (2.293 keV). In the maps, the presence of W outside the nanowire is a consequence of the proximity of peaks corresponding to different elements such as C-Kα (0.277 keV) and Au-Mα (2.12 keV). Therefore, in the maps corresponding to W and C elements, there is an increase of the amount of these elements on top of the metallic contact pads. The signal attributed to tungsten (W) in the low-energy region of the EDX spectrum ($\sim$ 0.2 keV), does not correspond to the typical characteristic lines of W, so it could be due to Bremsstrahlung effects or secondary fluorescence in elements in the vicinity such as C and O. The presence of O, Au or Si cannot be ignored as the contribution of the substrate at this acceleration voltage cannot be neglected. That is the reason why our results differ slightly to other research [10,11,13,45]. Considering just the ratio W/(W+C+Ga), the W % is in the range of $\sim$ 34 %.

We show the dynamic response to illumination in Fig. 7(a). After illuminatiom, the circuit is an RL circuit composed of the kinetic inductance (L_k) of the nanowire and the equivalent resistance of the readout circuit (R_{eq}). After the generation of a resistive region, the current redistributes between the shunt resistor (R_{shunt}) and the load resistance (R_L) of the readout circuit. According to the Kirchoff laws:

$$\sum V_i = 0 \tag{2}$$

$$L_k \frac{dI}{dt} + R_{eq} I = V_b \tag{3}$$

$$R_{eq} = \frac{R_L R_{shunt}}{R_L + R_{shunt}} \tag{4}$$

$$I(t) = I_b \left(1 - e^{-\frac{R_{eq}}{L_k} t} \right) \tag{5}$$

$$\tau_{fall} = \frac{L_k}{R_{eq}} \tag{6}$$

The derived $\tau_{rise} \sim 5.2\,ns$ and $\tau_{fall} \sim 7.2\,ns$ from the oscilloscope traces highlight the fast temporal response of the detector and suitability for high-speed detection applications. According to $\tau_{fall} = L_k/R_{eq}$ the kinetic inductance of the nanowire is $L_k \sim 180\,nH$ and the bandwith $1/2\pi(\tau_{rise} + \tau_{fall}) \sim 12.8\,MHz$. In our case the capacitance contributions from the bias-tee and the amplifier are negligible to the τ_{fall} compared to the kinetic inductance contribution. Since the transversal area of the nanowire is higher than in a typical SNSPD, the hotspot resistance (R_n) is lower. Therefore, the value of τ_{rise} is higher [46]. The detector speed is probably higher as the pulse width of the laser $\sim$ 4ns, as well as the jitter, are affecting the temporal rise time and decay constants. The timing jitter (Δt) is a variation in the time delay between photon absorption and the appearance of a photon count [47]. The jitter measured comprised the contribution of the jitter from the laser input, the sync

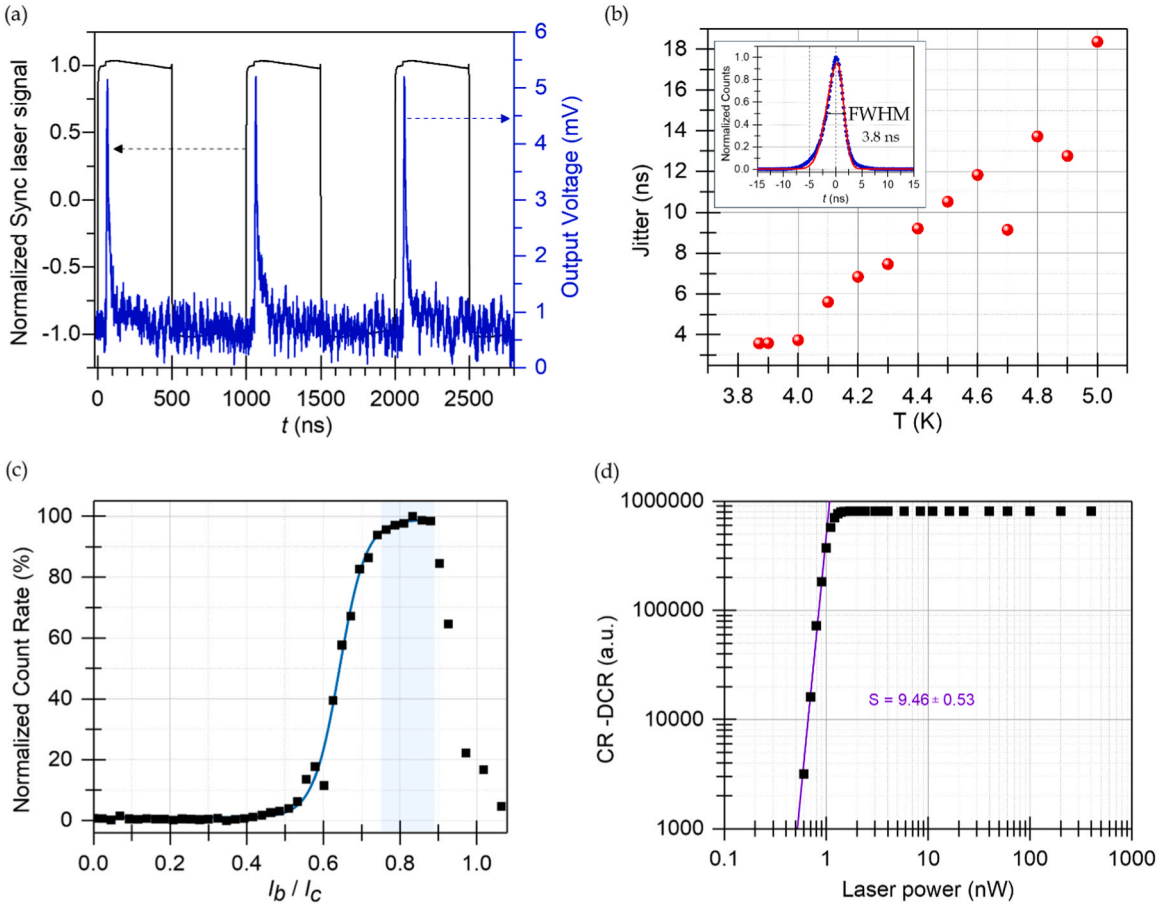

Fig. 7. (a) Oscilloscope trace displaying the normalized sync laser signal (black line, left axis) and the output voltage of the detector (blue line, right axis), as a function of time (t). The single-shot was averaged 5000 times. (b) Evolution of the total jitter with the temperature. The inset shows the normalized histogram of photon detection events at 3.8 K showing the total temporal jitter of the system ($FWHM \sim 3.8ns$). Experimental data (blue dots) is fitted with an asymmetric gaussian profile (red line). (c) Normalized count rate as a function of I_b/I_c at 1.5 nW of incident power at the entry window of the cryostat. (d) Count rate minus dark count rate (DCR) as a function of laser power. S value near 9.5 proves that close to 10 photons at 640 nm are required to trigger a measurable voltage bias output.

signal, the time-correlated photon counting adquisition card (TCSPC), the electronics and the nanowire itself:

$$(\Delta t)^2_{meas} = (\Delta t)^2_{laser} + (\Delta t)^2_{sync} + (\Delta t)^2_{TCSPC} + (\Delta t)^2_{elec} + (\Delta t)^2_{nw} \quad (7)$$

The inset in Fig. 7(b) shows the typical normalized histogram of photon detection events at 3.8 K, characteristic of the convoluted temporal response of the system. According to the central limit theorem, if the variability is purely random cand arises from independent sources, this distribution is approximately gaussian and symmetric. Since our histogram has been registered counting the detection events from the detector output (start) to the sync pulse of the laser (stop), an asymmetry to the left indicates that some events are registered faster than expected. This can be a consequence of the noise present in the threshold detection. For each of the measured IRFs (Instrument Response Functions) we fit an asymmetric gaussian function as shown in Fig. 7(b) and from the fitted functions extracted the total measurement jitter, defined as the FWHM of the IRF [48]. The asymmetric Gaussian fitting gives a $FWHM \sim 3.8\ ns$ jitter. In other research [47], part of the jitter has been attributed to the difference in the propagation time of the electrical signal across the strip from different locations when photons are absorbed in flood illumination schemes. Since in our experiment, the laser spot is focused in a particular point of the detector, the jitter observed may not be highly influenced by the size dependent jitter. The main contribution to the jitter comes from the nanowire itself. Considering that the nanowire is too thick for single-photon detection, more energy (multiple photons) may be required to induce a detection event. Consequently, the transition from the superconducting to the resistive state is more stochastic and slow. The operation temperature near Tc and the thermal latency, where energy gradually accumulates before triggering a response, are some of the reasons why the jitter value of our detector is higher than the values usually reported in SNSPDs. The expected increase of this jitter with the temperature is shown in Fig. 7(b), The dependence of the jitter with the temperature is analogous to the reported trend between jitter and I_b in other research [48]. The amplitude output pulses are higher (higher SNR) with increasing I_b, therefore the jitter decreases. The increase of the temperature is analogous to a decrease in I_b, because there is a reduction of I_c with the temperature (Fig. 5) as the Cooper pairs density (n_s) decreases.

The typical saturation characterization of an SNSPD is done by measuring the count rate (CR) at a fixed photon wavelength and a varying I_b. This saturation curve is widely reported in the literature of SNSPDs [48]. For higher I_b and/or photon energies, the photon count rate (PCR) is approximately constant (plateau) and below the threshold, the PCR rapidly decreases following and approximately exponential function. For monochromatic photons, the detection efficiency saturates when the current approaches the experimental (switching) current (I_{sw}), but deteriorates rapidly when the current decreases below the cut-off value [47,49]. The system detection efficiency is defined as:

$$SDE = (CR - BCR)/R_{in} \quad (8)$$

Where CR is the measured output count rate, BCR is the background count rate and R_{in} is the input photon flux. Given that our laser is not CW but pulsed and there are optical losses in our free-space set-up, we do not express SDE but the normalized difference $CR - BCR$, which is proportional to SDE and shows the same trend.

Fig. (7) (c) shows the evolution of the normalized count rate as a function of I_b/I_c. It shows a sigmoidal growth typically observed in SNSPD, where the count rate increases sharply as I_b approaches I_c, reflecting a higher probability of photon detection. The obtained experimental results indicate that the nanowires WC detector operates stably in the saturation range $(0.75 \leq I_b/I_c < 0.90)$ emphasizing the importance of precise bias current tuning for optimal performance. As the mechanism of photodetection resembles SNSPDs, the saturation plateau at 640 nm means that the system could be suitable for IR wavelength. In that case, the saturation plateau is expected to be reached at higher I_b. Although this threshold current could be moved to lower values if the transversal section of the nanowire decreases [50]. Furthermore, this experiment has been carried out without control on the polarization. Since SNSPDs have a polarization dependency [49], we expect that the detection efficiency of the system improves by the use of polarizers.

At very low photon fluxes, in SNSPDs the single-photon detection regime has been extensively reported with a slope $S = 1$ in the curve between the PCR and the incident photon flux [48,51]. This demonstration has been extensively explained in this paper[52]. According to this, in the "hot-spot" model, the n-photon counts result from the appearance of n hotspots where n photons are absorbed in a small region of the superconducting detector. The simultaneous absorption of n photons in one square of the strip follows a Poisson distribution:

$$P(n) = \frac{\langle n \rangle^n e^{-\langle n \rangle}}{n!} \quad (9)$$

Where $\langle n \rangle = Am/N_{sq}$ is the mean number of photons absorbed in one square of the strip, A is the absorption coefficient and m is the mean number of photons in an optical pulse. The PCR in the n-photon regime is [52]:

$$CR^{(n)}(m) = \left(\frac{\upsilon \eta^n A^n}{N_{sq}^{n-1} n!}\right) m^n \quad (10)$$

Where ν is the pulse repetition rate and η is the quantum efficiency. The probability of a n-photon count by the detector will equall the sum of the probabilities of each square [52]:

$$CR(m) = \sum c_i m^i \quad (11)$$

In the linear photon regime, the count rate of photons will be proportional to $m(i = 1)$.Fig. 7(d) follows the evolution of the count rate after subtracting the background count rate (BCR) versus the laser power measured at the entrance of the cryostat. At low illumination powers, the detector operates efficiently without saturation and is sensitive to the incident energy. Considering a linear dependency of the laser power before reaching saturation, $S > 1$ indicates that the detector needs to absorb multiple photons to reach a thermal threshold for a hotspot formation. Our CR dependence is highly non-linear, showing a multiphoton absorption. This behavior at low illumination powers is a consequence of both the increase of probability of a many-photon detection process and the device limited sensitivity to low photon fluxes [51]. When the energy of one photon is not sufficient to generate a light count, multiphoton detection events may occur. If several photons are absorbed within the lifetime of the hotspot, τ_{HS}, at a distance from each other less than the diameter of the hotspot and their total energy is large enough, a count does occur [47]. This is highly likely to happen in this research since the laser spot is focused in a particular region of the nanowire. Although the size of the hotspot is poorly quantified in the literature for W and other superconductors [47], its radius (R) can be roughly related with the energy of the absorbed photon as:

$$\eta \frac{ch}{\lambda} \cong d\pi R^2 \frac{H_{cm}^2}{8\pi} \quad (12)$$

Where the coefficient $0 < \eta < 1$ takes into account that only part of the energy of the photon is delivered for suppression of Δ, and the rest of the photon's energy heats the quasiparticles and phonons. $H_{cm}^2/8\pi$ is the superconducting condensation energy per unit of volume and $H_{cm} = \left(\phi_0/2\sqrt{2}\,\pi\xi\lambda_L^2\right)$ is the thermodynamic magnetic field. In the hard-core spot model (49), the maximum radius of the normal hotspot is:

$$R_n = \left(\frac{\eta h\nu}{\pi d N_0 \Delta^2}\right)^{1/2} \quad (13)$$

Where d is the thickness, N_0 is the density of electronic states in the film

at the Fermi level per one spin and η is the fraction of the photon energy delivered to electrons ($\eta < 1$) [47]. The lower the thickness, the larger the hotspot size. Since our thickness is many times higher than ξ, these WC-FIBID nanowires become effectively non-sensitive to single photons. Only the cumulative effect of many photons can be seen. When the energy absorbed by multiple photon in one pulse overcomes the threshold to create a resistance high enough to deviate the current to the readout circuit, it generates an event of detection. At high illumination power, all laser pulses are generating detection and the detector cannot respond to anymore. Thus, *CR* stops growing despite increasing laser power and $S \approx 0$.

In our case, an S value or 9.46 ± 0.53 proves that the nanowire requires 9–10 photons at 640 nm to generate a sufficiently large hot-spot and create a measurable voltage bias output pulse.

Finally, Fig. 8 shows in-operando low-temperature (3.8 K) photoresponse maps showing the DC-signal output of the lock-in amplifier when the detector is scanned under 1 MHz laser illuminated at different powers and different I_b. Thanks to this method, the electrical noise contribution can be discarded, and the lateral resolution enables the visualization of hot-spot distribution. In our photoresponse maps we do not visualize the "hot-spots" distribution, understanding the "hot-spot" as the region with non-zero resistance that arises from the absorption of a photon but after the absorption of multiple photons. These maps reveal the local suppression of superconductivity under photon absorption and the evolution of the detector response as I_b approaches and surpasses I_c. This lateral resolution allows to distinguish regions of the nanowire with different detection efficiencies, even some blind sections of the nanowire are low I_b values. At $I_b \sim 0.63\, I_c$, there is little appreciable response in the nanowire, and it sharply increases as it approaches I_c. Near I_c, it is possible to see some regions where superconductivity is still present and detect incoming light. There has been experimental indication that the detection threshold is position dependent. The detection threshold current for a given photon energy depends on the absorption position along the cross-section of the nanowire [53]. The nanowire has inhomogeneities, such as structural defects and variations in thickness and/or width [54]. It has been demonstrated that the performance of SNSPDs critically depends on the local inhomogeneity and spatial variations of the superconducting properties of the material. The slighlest degree of disorder, leads to a variation in the superconducting gap and T_c [55]. The different variation from the regions with higher and lower response is probably due to the variation of the I_c and superconducting order parameter (Δ) [55]. Physically, this implies that Δ should control the PCR [53]. Similarly to this research, where they show the correlation of local suppression of superconductivity by STM with inhomogeneity, in this research we observe the local suppression of superconductivity by illumination. As the SEM and AFM images show variations on width and thickness, and they have an impact in the degree of suppression of superconductivity, we infer that these inhomogeneities lead to regions with more or less detection efficiency. As these nanowires do not operate in the single-photon regime it would be interesting in the future to develop a mix model that takes into account bolometric effects in SNSPDs.

4. Conclusions

We have successfully grown tungsten carbide nanowires by FIBID with a thickness as low as 50 nm using 5 keV Ga^+ focused ion beam and $W(CO)_6$ as the precursor. The nanowire exhibits a room-temperature resistivity of 243 μΩ.cm and superconducting properties, including a $T_c > 4.5$ K, a transition width of 0.82 K and a $J_c \sim (0.93 \pm 0.36).10^5 A/cm^2$. These results are comparable to those reported in previous studies [24]. The resistive tail observed below Tc can be attributed to an incomplete superconducting transition, as well as to contact resistance, vortex and contribution from phase slips. The critical current follows Bardeen theory suggesting that the deposits are well-described by the BCS superconductivity model at least near T_c. The chemical composition analysis confirms that the nanowires are composed of W, C, O, and Ga, which is consistent with the typical characteristics of WC-FIBID grown materials.

Despite earlier suggestions that WC-based FIBID SNSPDs could be fabricated [24], to the best of our knowledge this has not been experimentally demonstrated yet. In this research, we have shown the electrical response of the nanowires under low-intensity illumination. Using a lock-in scanning technique, we achieved great spatial resolution enabling the visualization of hot-spots distribution. This capability can be further exploited to identify areas of the nanowire with the highest detection efficiency, as well as potential defects or constrictions. Preliminary studies of jitter, detection efficiency and detector speed suggest promising behavior under illumination. The linear regime in log-scale observed at low illumination power indicates sensitivity to incident energy without saturation. However, the power dependency ($S > 1$) suggests that multiple photons may need to be absorbed to reach the thermal threshold for a single hot-spot formation, which can trigger a detection event. These findings are consistent with the quasi-2D nature of the detector, where neither the width nor the thickness is smaller than the coherence length (ξ). It is well established that single-photon

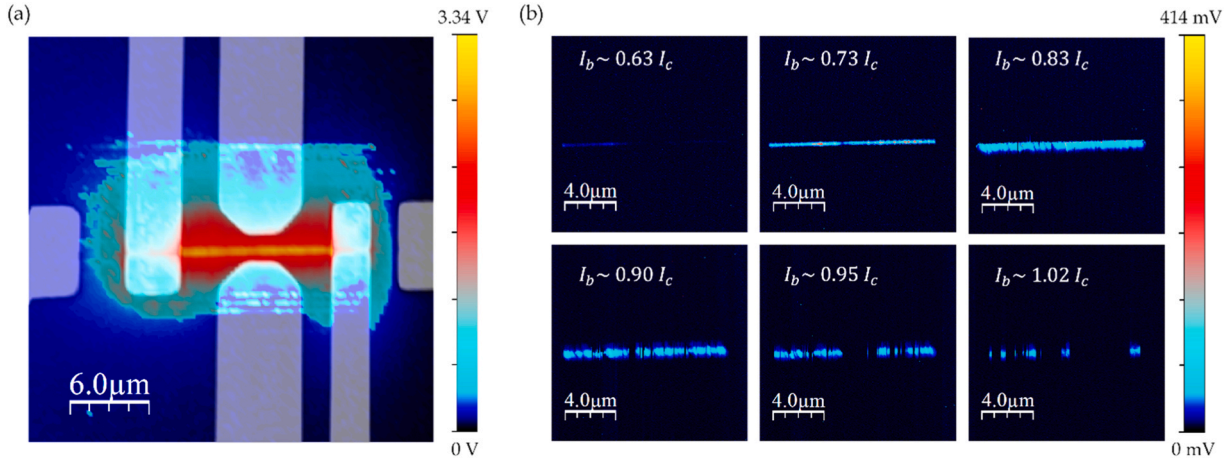

Fig. 8. Photoresponse maps of the detector showing the hot-spot distribution at high optical power (1 μW) (a) and 600 pW (b). In image (a) there is an overlayed image of the reflectance map of the sample, which is obtained simultaneously to the scanning process (See supplementary, S2). The main electrical response appears between the inner contact pads where the current is flowing. The response around the nanowire at high illumination powers can be a consequence of thermal effects and back-reflections from the metallic pads. (b) image is taken as a zoomed image in the central region of the nanowire between the two inner pads at different I_b.

detectors and phase-slip qubits require ultrathin superconducting films [12]. Our results indicate that further reduction in thickness below 25 nm would be necessary for these nanowires to be fully suitable for these applications [6,12,39].

In conclusion, we demonstrated the significant potential of WC-FIBID grown nanowires for advanced superconducting photon detection applications with further refinements in material properties and thickness required for optimal performance.

CRediT authorship contribution statement

Granados Daniel: Writing – original draft, Validation, Supervision, Resources, Project administration, Methodology, Investigation, Funding acquisition, Data curation, Conceptualization. **García-Pérez Cristina:** Writing – original draft, Validation, Software, Methodology, Investigation, Data curation. **Urbanos Fernando J:** Writing – review & editing, Methodology, Investigation. **Caballero Gabriel:** Methodology, Investigation. **Osorio Manuel R.:** Writing – review & editing, Methodology, Investigation. **Gómez Alicia:** Writing – review & editing, Methodology, Investigation, Funding acquisition, Formal analysis, Conceptualization. **Bernardo-Gavito Ramón:** Writing – review & editing, Validation, Supervision, Software, Project administration, Methodology, Investigation, Funding acquisition, Formal analysis, Data curation.

Author contributions

D.G., R.B-G., and A.G. conceived the idea, conducted the general research, and secured financial support. C.G. designed the experiments, performed the electrical and optoelectrical measurements, and analyzed the data. D.G., F.J., and M.R. fabricated the devices, while G.C. conducted the A.F.M. experiments. D.G. and R.B. supervised and managed the research project. All authors contributed to discussing the results. The manuscript was written by C.G., with revisions and improvements by D.G. and R.B., and contributions from all authors.

Declaration of Generative AI and AI-assisted technologies in the writing process

During the preparation of this work the author(s) used CHAT GPT 4.0 PRO in order to improve our non-native English grammar and spelling. After using this tool/service, the author(s) reviewed and edited the content as needed and take(s) full responsibility for the content of the publication.

Competing interests

The authors declare no competing interests.

Declaration of Competing Interest

The authors declare that they have no known competing financial interests or personal relationships that could have appeared to influence the work reported in this paper.

Acknowledgements

This work is partially supported by the Comunidad de Madrid through Grant MAD4SPACE-CM TEC-2024/TEC-182 and 2019-T2/IND-13367 (R.B.-G.). IMDEA Nanociencia thanks support from the "Severo Ochoa'' program for Centers of Excellence in R&D (MINECO, Grant CEX2020–001039-S). This work was also supported by grants, FPU20/05794 and PID2022–137779OB-C42. We also acknowledge financial support from ONR-Global under Grant DEFROST N62909–19–1–2053.

Appendix A. Supporting information

Supplementary data associated with this article can be found in the online version at doi:10.1016/j.mtquan.2025.100043.

Data Availability

Data will be made available on request.

References

[1] P. Orús, F. Sigloch, S. Sangiao, J.M. De Teresa, Superconducting materials and devices grown by focused ion and electron beam induced deposition, Nanomaterials 12 (2022), https://doi.org/10.3390/nano12081367.
[2] J. Basset, D. Watfa, G. Aiello, M. Féchant, A. Morvan, J. Estève, et al., High kinetic inductance microwave resonators made by He-Beam assisted deposition of tungsten nanowires, Appl. Phys. Lett. 114 (2019), https://doi.org/10.1063/1.5080925.
[3] C.M. Natarajan, M.G. Tanner, R.H. Hadfield, Superconducting nanowire single-photon detectors: physics and applications, Supercond. Sci. Technol. 25 (2012), https://doi.org/10.1088/0953-2048/25/6/063001.
[4] I. Chiorescu, et al., Coherent quantum dynamics of a superconducting flux qubit, Science 299 (1979) (2003) 1869–1871.
[5] P. Orús, V.M. Fomin, J.M. De Teresa, R. Córdoba, Critical current modulation induced by an electric field in superconducting tungsten-carbon nanowires, Sci. Rep. 11 (2021), https://doi.org/10.1038/s41598-021-97075-z.
[6] J.E. Mooij, Y.V. Nazarov, Superconducting nanowires as quantum phase-slip junctions, Nat. Phys. 2 (2006) 169–172, https://doi.org/10.1038/nphys234.
[7] P. Orús, R. Córdoba, G. Hlawacek, J.M. De Teresa, Superconducting properties of in-plane W-C nanowires grown by He+ focused ion beam induced deposition, Nanotechnology 32 (2020) 085301.
[8] I.J. Luxmoore, I.M. Ross, A.G. Cullis, P.W. Fry, J. Orr, P.D. Buckle, et al., Low temperature electrical characterisation of tungsten nano-wires fabricated by electron and ion beam induced chemical vapour deposition, Thin Solid Films 515 (2007) 6791–6797, https://doi.org/10.1016/j.tsf.2007.02.029.
[9] F. Porrati, S. Barth, R. Sachser, O.V. Dobrovolskiy, A. Seybert, A.S. Frangakis, et al., Crystalline niobium carbide superconducting nanowires prepared by focused ion beam direct writing, ACS Nano 13 (2019) 6287–6296, https://doi.org/10.1021/acsnano.9b00059.
[10] E.S. Sadki, S. Ooi, K. Hirata, Focused-ion-beam-induced deposition of superconducting nanowires, Appl. Phys. Lett. 85 (2004) 6206–6208, https://doi.org/10.1063/1.1842367.
[11] W. Li, J.C. Fenton, Y. Wang, D.W. McComb, P.A. Warburton, Tunability of the superconductivity of tungsten films grown by focused-ion-beam direct writing, J. Appl. Phys. 104 (2008), https://doi.org/10.1063/1.3013444.
[12] W. Li, J.C. Fenton, P.A. Warburton, Focused-ion-beam direct-writing of ultra-thin superconducting tungsten composite films, IEEE Trans. Appl. Supercond. 19 (2009) 2819–2822, https://doi.org/10.1109/TASC.2009.2019251.
[13] J. Dai, K. Onomitsu, R. Kometani, Y. Krockenberger, H. Yamaguchi, S. Ishihara, et al., Superconductivity in tungsten-carbide nanowires deposited from the mixtures of W(CO)6 and H14H10, Jpn J. Appl. Phys. 52 (2013), https://doi.org/10.7567/JJAP.52.075001.
[14] I. Guillamón, H. Suderow, S. Vieira, A. Fernández-Pacheco, J. Sesé, R. Córdoba, et al., Nanoscale superconducting properties of amorphous W-based deposits grown with a focused-ion-beam, N. J. Phys. 10 (2008), https://doi.org/10.1088/1367-2630/10/9/093005.
[15] N. Bassim, K. Scott, L.A. Giannuzzi, Recent advances in focused ion beam technology and applications, MRS Bull. 39 (2014) 317–325, https://doi.org/10.1557/mrs.2014.52.
[16] Matsui S., Ochiai Y. Focused ion beam applications to solid state devices. n.d.
[17] Puers R., Reyntjens S. Fabrication and testing of custom vacuum encapsulations deposited by focused ion beam direct-write CVD. n.d.
[18] A.J. De Marco, J. Melngailis, Maskless fabrication of JFETs via focused ion beams, Solid State Electron 48 (2004) 1833–1836, https://doi.org/10.1016/j.sse.2004.05.022.
[19] I.J. Luxmoore, I.M. Ross, A.G. Cullis, P.W. Fry, J. Orr, P.D. Buckle, et al., Low temperature electrical characterisation of tungsten nano-wires fabricated by electron and ion beam induced chemical vapour deposition, Thin Solid Films 515 (2007) 6791–6797, https://doi.org/10.1016/j.tsf.2007.02.029.
[20] W. Li, J.C. Fenton, C. Gu, P.A. Warburton, Superconductivity of ultra-fine tungsten nanowires grown by focused-ion-beam direct-writing, Micro Eng. 88 (8) (2011) 2636, https://doi.org/10.1016/j.mee.2010.12.116.
[21] M. Mongillo, L. Jansen, G. Audoit, R. Berthier, D. Cooper, Electronic transport on W-rich films deposited by focused ion beam, J. Supercond. Nov. Magn. 30 (2017) 2261–2270, https://doi.org/10.1007/s10948-017-4028-2.
[22] Y. Sun, J. Wang, W. Zhao, M. Tian, M. Singh, M.H.W. Chan, Voltage-current properties of superconducting amorphous tungsten nanostrips, Sci. Rep. 3 (2013), https://doi.org/10.1038/srep02307.
[23] F. Porrati, L. Keller, C. Gspan, H. Plank, M. Huth, Electrical transport properties of Ga irradiated W-based granular nanostructures, J. Phys. D. Appl. Phys. 50 (2017), https://doi.org/10.1088/1361-6463/aa6bdb.
[24] R.P. Aloysius, S. Husale, A. Kumar, F. Ahmad, A.K. Gangwar, G.S. Papanai, et al., Superconducting properties of tungsten nanowires fabricated using focussed ion

beam technique, Nanotechnology 30 (2019), https://doi.org/10.1088/1361-6528/ab2d6d.
[25] H. Langfischer, B. Basnar, H. Hutter, E. Bertagnolli, Evolution of tungsten film deposition induced by focused ion beam, J. Vac. Sci. Technol. A: Vac., Surf., Films 20 (2002) 1408–1415, https://doi.org/10.1116/1.1486230.
[26] I. Guillamón, H. Suderow, A. Fernández-Pacheco, J. Sesé, R. Córdoba, J.M. De Teresa, et al., Direct observation of melting in a two-dimensional superconducting vortex lattice, Nat. Phys. 5 (2009) 651–655, https://doi.org/10.1038/nphys1368.
[27] I. Golokolenov, A. Guthrie, S. Kafanov, Y.A. Pashkin, V. Tsepelin, On the origin of the controversial electrostatic field effect in superconductors, Nat. Commun. 12 (2021), https://doi.org/10.1038/s41467-021-22998-0.
[28] M.T. Mercaldo, P. Solinas, F. Giazotto, M. Cuoco, Electrically tunable superconductivity through surface orbital polarization, Phys. Rev. Appl. 14 (2020), https://doi.org/10.1103/PhysRevApplied.14.034041.
[29] L. Chirolli, T. Cea, F. Giazotto, Impact of electrostatic fields in layered crystalline BCS superconductors, Phys. Rev. Res 3 (2021), https://doi.org/10.1103/PhysRevResearch.3.023135.
[30] P. Solinas, A. Amoretti, F. Giazotto, Sauter-Schwinger Effect in a Bardeen-Cooper-Schrieffer Superconductor, Phys. Rev. Lett. 126 (2021), https://doi.org/10.1103/PhysRevLett.126.117001.
[31] F. Paolucci, G. De Simoni, P. Solinas, E. Strambini, N. Ligato, P. Virtanen, et al., Magnetotransport experiments on fully metallic superconducting dayem-bridge field-effect transistors, Phys. Rev. Appl. 11 (2019), https://doi.org/10.1103/PhysRevApplied.11.024061.
[32] F. Paolucci, F. Vischi, G. De Simoni, C. Guarcello, P. Solinas, F. Giazotto, Field-effect controllable metallic josephson interferometer, Nano Lett. 19 (9) (2019) 6263, https://doi.org/10.1021/acs.nanolett.9b02369.
[33] De Teresa J.M., Fernández-Pacheco A., Córdoba R., Sesé J., Ibarra M.R., Guillamón I., et al. Transport properties of superconducting amorphous W-based nanowires fabricated by focused-ion-beam-induced-deposition for applications in Nanotechnology. 2009.
[34] M. Tinkham. Introduction to Superconductivity, Second ed., The McGraw-Hill, New York, 1996.
[35] B.I. Halperin, G. Refael, E. Demler, Resistance in superconductors, Int J. Mod. Phys. B 24 (2010) 4039–4080, https://doi.org/10.1142/S021797921005644X.
[36] I. Guillamón, H. Suderow, S. Vieira, A. Fernndez-Pacheco, J. Sesé, R. Córdoba, et al., Superconducting density of states at the border of an amorphous thin film grown by focused-ion-beam, in: J Phys Conf Ser, 150, Institute of Physics Publishing, 2009, https://doi.org/10.1088/1742-6596/150/5/052064.
[37] N. Shah, D. Pekker, P.M. Goldbart, Inherent stochasticity of superconductor-resistor switching behavior in nanowires, Phys. Rev. Lett. 101 (2008), https://doi.org/10.1103/PhysRevLett.101.207001.
[38] W.J. Skocpol, M.R. Beasley, M. Tinkham, Self-heating hotspots in superconducting thin-film microbridges, J. Appl. Phys. 45 (1974) 4054–4066, https://doi.org/10.1063/1.1663912.
[39] Quantum suppression of superconductivity in ultrathin nanowires n.d..
[40] P. Dhakal, G. McMahon, S. Shepard, T. Kirkpatrick, J.I. Oh, M.J. Naughton, Direct-write, focused ion beam-deposited, 7 K superconducting C-Ga-O nanowire, Appl. Phys. Lett. 96 (2010), https://doi.org/10.1063/1.3458863.
[41] C.N. Lau, N. Markovic, M. Bockrath, A. Bezryadin, M. Tinkham, Quantum phase slips in superconducting nanowires, :217003-1-217003–4, Phys. Rev. Lett. 87 (2001), https://doi.org/10.1103/PhysRevLett.87.217003.
[42] P. Li, P.M. Wu, Y. Bomze, I.V. Borzenets, G. Finkelstein, A.M. Chang, Switching currents limited by single phase slips in one-dimensional superconducting Al nanowires, Phys. Rev. Lett. 107 (2011), https://doi.org/10.1103/PhysRevLett.107.137004.
[43] M. Sahu, M.H. Bae, A. Rogachev, D. Pekker, T.C. Wei, N. Shah, et al., Individual topological tunnelling events of a quantum field probed through their macroscopic consequences, Nat. Phys. 5 (2009) 503–508, https://doi.org/10.1038/nphys1276.
[44] J. Bardeen, Critical fields and currents in superconductors, Rev. Mod. Phys. 34 (1962) 667–681.
[45] I.J. Luxmoore, I.M. Ross, A.G. Cullis, P.W. Fry, J. Orr, P.D. Buckle, et al., Low temperature electrical characterisation of tungsten nano-wires fabricated by electron and ion beam induced chemical vapour deposition, Thin Solid Films 515 (2007) 6791–6797, https://doi.org/10.1016/j.tsf.2007.02.029.
[46] J.A. Lau, V.B. Verma, D. Schwarzer, A.M. Wodtke, Superconducting single-photon detectors in the mid-infrared for physical chemistry and spectroscopy, Chem. Soc. Rev. 52 (2023) 921–941, https://doi.org/10.1039/d1cs00434d.
[47] A.D. Semenov, Superconducting nanostrip single-photon detectors some fundamental aspects in detection mechanism, technology and performance, Supercond. Sci. Technol. 34 (2021), https://doi.org/10.1088/1361-6668/abef7d.
[48] Vyhnalek B.E., Tedder S.A., Nappier J.M. Performance and characterization of a modular superconducting nanowire single photon detector system for space-to-Earth optical communications links. n.d.
[49] Vyhnalek B.E., Tedder S.A., Katz E.J., Nappier J.M. Few-mode fiber coupled superconducting nanowire single-photon detectors for photon efficient optical communications. n.d.
[50] Azem A., Morozov D.V., Kuznesof D., Bruscino C., Hadfield R.H., Chrostowski L., et al. Mid-infrared characterization of NbTiN superconducting nanowire single-photon detectors on silicon-on-insulator 2024. https://doi.org/10.1063/5.0237005.
[51] A. Verevkin, J. Zhang, R. Sobolewski, A. Lipatov, O. Okunev, G. Chulkova, et al., Detection efficiency of large-active-area NbN single-photon superconducting detectors in the ultraviolet to near-infrared range, Appl. Phys. Lett. 80 (2002) 4687–4689, https://doi.org/10.1063/1.1487924.
[52] M.S. Elezov, A.V. Semenov, P.P. An, M.A. Tarkhov, G.N. Goltsman, A.I. Kardakova, et al., Investigating the detection regimes of a superconducting single-photon detector, J. Opt. Technol. 80 (2013) 435, https://doi.org/10.1364/jot.80.000435.
[53] A. Engel, J.J. Renema, K. Il'In, A. Semenov, Detection mechanism of superconducting nanowire single-photon detectors, Supercond. Sci. Technol. 28 (2015), https://doi.org/10.1088/0953-2048/28/11/114003.
[54] A.N. Zotova, D.Y. Vodolazov, Intrinsic detection efficiency of superconducting nanowire single photon detector in the modified hot spot model, Supercond. Sci. Technol. 27 (2014), https://doi.org/10.1088/0953-2048/27/12/125001.
[55] P.J. Chen, G.H. Chen, R. Vedin, M. Jönsson, S. Gyger, S. Steinhauer, et al., Visualizing local superconductivity of NbTiN nanowires to probe inhomogeneity in single-photon detectors, ACS Appl. Opt. Mater. 2 (2024) 68–75, https://doi.org/10.1021/acsaom.3c00326.